Scilight

Photocatalysis

https://www.sciltp.com/journals/photocatalysis

Supplementary Materials

Photocatalytic Hydrogen Generation over Natural Sepiolite and Palygorskite

Patrik Kopčan [1,2], Alexandr Martaus [1] and Kamila Kočí [1,3,*]

[1] Institute of Environmental Technology, Center for Energy and Environmental Technology, VŠB-Technical University of Ostrava, 70800 Ostrava, Czech Republic
[2] Faculty of Materials Science and Technology, VŠB-Technical University of Ostrava, 70800 Ostrava, Czech Republic
[3] Department of Physics and Materials Engineering, Faculty of Technology, Tomáš Baťa University in Zlín, 76001 Zlín, Czech Republic
* Correspondence: kamila.koci@vsb.cz

1. Materials and Methods

Photocatalytic Hydrogen Evolution Experiments

Photocatalytic H_2 evolution experiments were performed in a batch photoreactor (stainless steel, volume 305 cm^3). A detailed description of the photocatalytic experiment is provided in the Supplementary Materials.

Photocatalytic activity was tested in a stirred batch photoreactor constructed from stainless steel with a total internal volume of 305 mL. The reaction mixture consisted of 100 mL of a 50% *v*/*v* aqueous methanol solution with 0.1 g of the tested sample. Prior to irradiation, the suspension was purged with helium gas for 30 min at a pressure of 1250–1300 kPa to remove residual air.

A UVP Pen-Ray® low-pressure mercury lamp (Model 11SC-1, Analytik Jena GmbH + Co. KG, Germany; 8 W; λ_{max} = 254 nm) was placed vertically in a central quartz tube immersed in the photoreactor to provide UV-C irradiation. The system was stirred continuously. The emission spectrum of the UVP Pen-Ray® low-pressure mercury lamp employed in this study is shown in Figure S1.

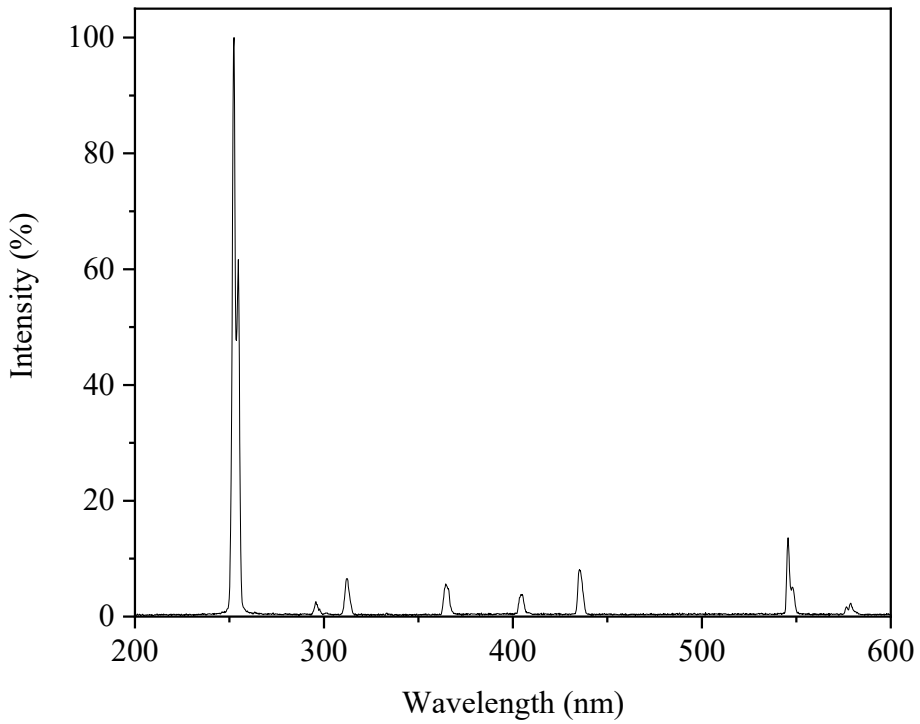

Figure S1. Emission spectrum of the UVP Pen-Ray® low-pressure mercury lamp employed in this study.

Photocatalytic tests were conducted for (i) a fresh sample and (ii) the same material after a 24 h long pre-irradiation, followed by a 4-h measurement in 1-h intervals. All experiments were performed at least triplicate to ensure reproducibility. Dark control experiments were also carried out by leaving the sample present in the aqueous methanol under otherwise identical conditions without UV exposure for 24 h. In addition, photolysis control experiments were performed under identical irradiation conditions in water–methanol mixtures without any photocatalyst present, in order to assess the intrinsic hydrogen yield arising solely from photolysis of aqueous methanol and water. The corresponding results are shown in Figure S2.

Hydrogen production was monitored via gas chromatography using a Shimadzu Tracera GC-2010 Plus equipped with a Barrier Discharge Ionization Detector (BID) and a molecular sieve 5A column. Gas samples were collected at fixed time intervals and injected directly. Results are reported as cumulative hydrogen concentration (μmol H_2 per gram of photocatalyst).

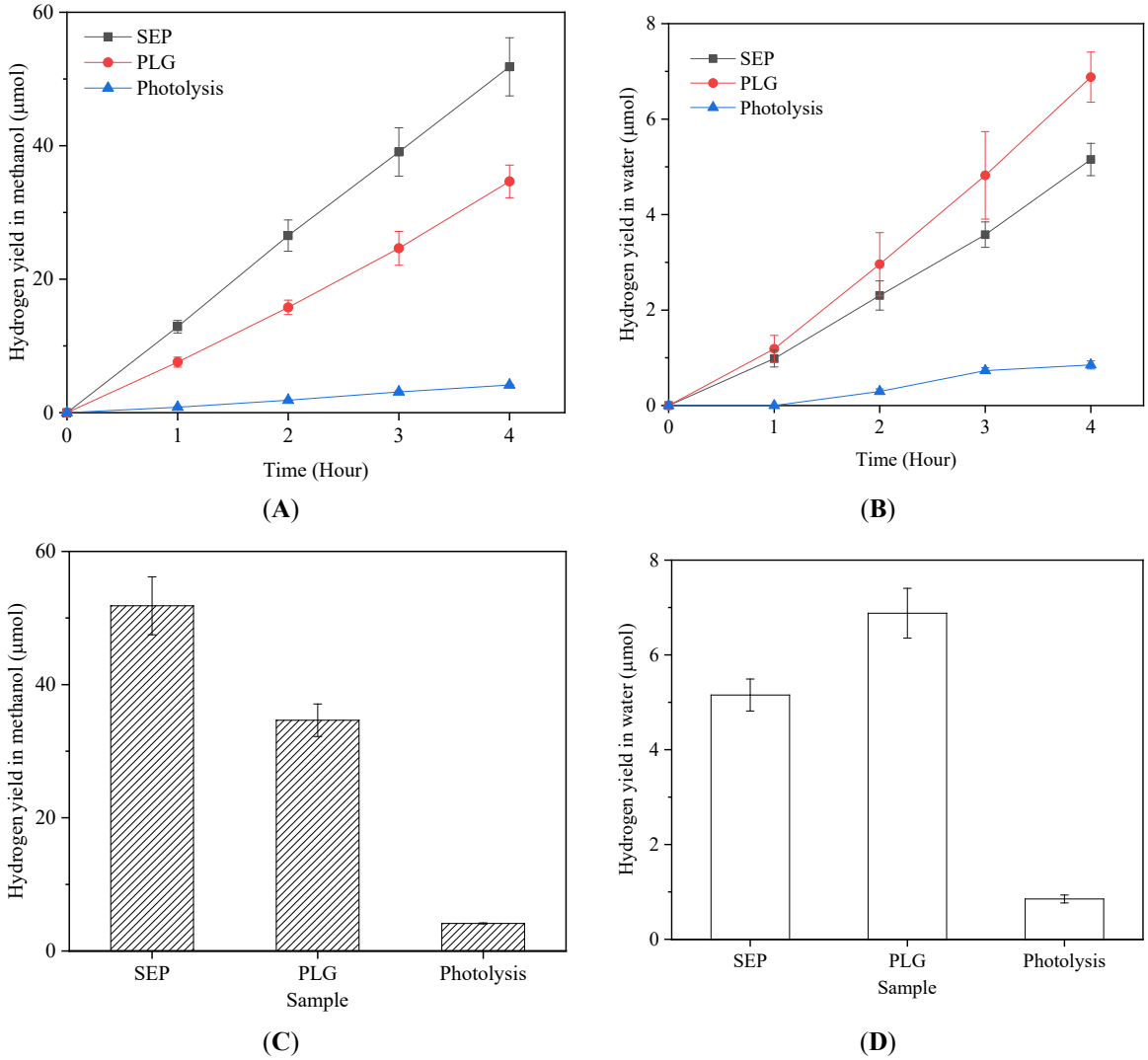

Figure S2. Time-dependent hydrogen evolution during photolysis and photocatalysis in aqueous methanol (**A**) and water (**B**) under continuous UV-C irradiation (λ = 254 nm) and comparison of total hydrogen yields obtained after 4 h in case of photolysis and photocatalysis in aqueous methanol (**C**) and water (**D**).

2. Results & Discussion

2.1. X-Ray Diffraction (XRD) & X-Ray Fluorescence (XRF)

The mineralogical composition of the studied clay samples was assessed by X-ray diffraction (XRD), while their elemental composition was examined by X-ray fluorescence (XRF). This combined approach enabled identification of the principal crystalline phases together with semiquantitative evaluation of the major and minor elements present in the materials. The XRD patterns of natural sepiolite (SEP) and palygorskite (PLG) are shown in Figure S3.

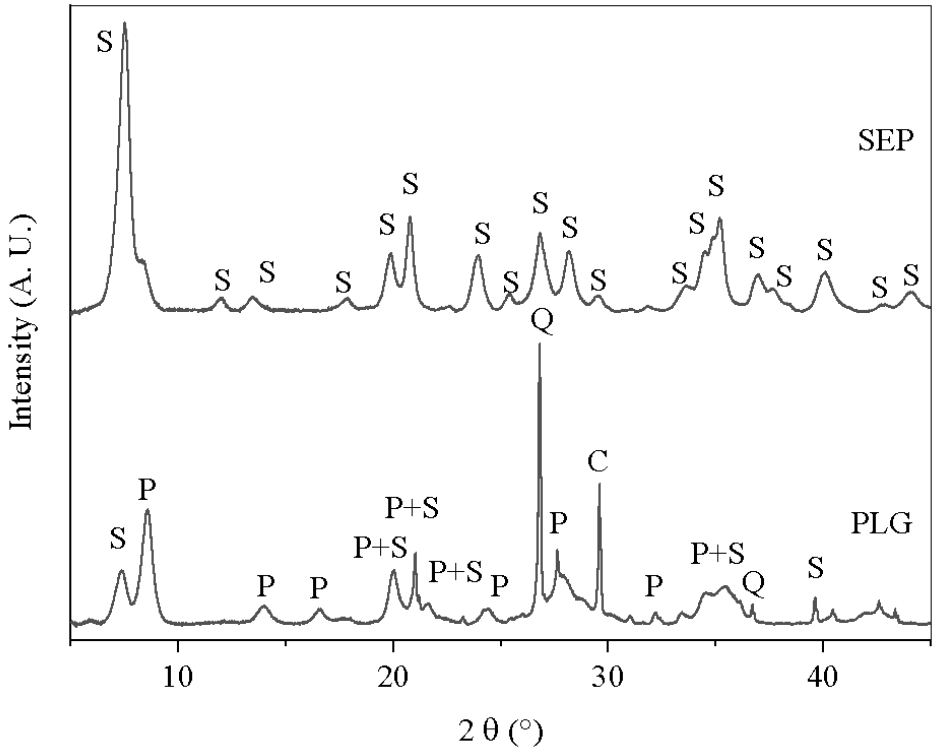

Figure S3. Powder X-ray diffraction patterns of natural sepiolite (SEP) and palygorskite (PLG) sample (C-calcite, P-palygorskite, Q-quartz, S-sepiolite).

2.2. Fourier-Transform Infrared (FTIR) Spectrometry

2.2.1. Sepiolite (SEP)

Sepiolite shows a reversible, adsorption-driven response with no framework damage. In the O–H region, the weak structural octahedral M–OH shoulder near ~3685 cm^{-1} remains unchanged [1–3]. Hydration-sensitive features attributed to coordinated/edge water (~3620 and ~3560 cm^{-1}) increase at 24 h and partially relax by 72 h [2,4,5]. The zeolitic/adsorbed-water envelope (centered ~3430 and ~3260 cm^{-1}) likewise grows at 24 h and diminishes toward the native level by 72 h, with a slight red-shift toward ~3300 cm^{-1} indicating more strongly H-bonded channel water [3,5,6]. Weak aliphatic C–H bands (2950–2850 cm^{-1}) appear at 24 h and recede by 72 h, consistent with transient adsorption of methanol-derived organics; no persistent carbonyl group vibration growth is observed in 1730–1700 cm^{-1}. The H–O–H bend (~1700–1630 cm^{-1}) follows the same reversible pattern [1,4,5,7,8]. Carbonate signatures are not detected above threshold and no δCO_3 appears near ~880 cm^{-1}) [9,10]. The framework region is invariant: ν_{as}(Si–O–Si) (~1250–1190 cm^{-1}), ν(Si–O) (~1080; ~1020, 980 cm^{-1}) and lattice modes (~780, 690–650, 540 cm^{-1}) show stable positions and shapes [2–5,11,12]. Quantitatively, the integrated O–H area rises from 120.9 (native) to 191.4 (24 h), then relaxes to 141.5 (72 h); the water-only reference (SEP_Blank_24H) is 133.9. We use the O–H band full width at half maximum (FWHM) as a compact proxy for H-bond–strength distribution (surface heterogeneity): it narrows from 386.3 cm^{-1} (native) to 355.6 cm^{-1} (24 h), indicating a more uniform OH population after cleaning, then partially re-broadens to 374.3 cm^{-1} (72 h)—with the water-only reference at 385.2 cm^{-1}—consistent with rehydration/adsorbate-induced heterogeneity. Overall, SEP undergoes temporary channel/edge hydration with transient organic adsorption and partial self-cleaning by 72 h. Quantitatively, the integrated O–H

area rises from 120.9 (native) to 191.4 (24 h) before decreasing to 141.5 (72 h); the water-only reference is 133.9. The O–H FWHM narrows from 386.3 cm^{-1} (native) to 355.6 cm^{-1} (24 h) and partially rebounds to 374.3 cm^{-1} (72 h); the water-only reference is native-like 385.2 cm^{-1}. Together, this indicates transient over-hydration of channels/edges in aqueous methanol with co-adsorbed, alcohol-derived species forming a relatively ordered H-bond network at 24 h (narrower band), followed by partial desorption/oxidation by 72 h that lowers total O–H and re-introduces heterogeneity. The water-only reference blank, lacking methanol, gives moderate loading and native-like breadth. Comparison of SEP's FTIR and XRD shows that the observed changes are surface driven, with no evidence of lattice modification.

2.2.2. Palygorskite (PLG)

PLG exhibits a reversible, adsorption-controlled evolution with no framework damage. The structural octahedral M–OH shoulder near ~3685 cm^{-1} is stationary [2,13–15], while coordinated/edge-water features at ~3620 and ~3560 cm^{-1} increase from 24 h to 72 h [2,13,14,16]. The zeolitic/adsorbed-water envelope shows two main components near ~3440 and ~3300 cm^{-1} and grows with a slight low-frequency asymmetry, consistent with stronger H-bonding [13–16]. The ~3300 cm^{-1} band, attributed to strongly H-bonded zeolitic water in the tunnels—distinct from coordinated water and structural OH [15–17]; is strongest in the water-only reference (PLG_Blank_24H) and remains detectable after both 24 h and 72 h in aqueous methanol, while significantly weaker, consistent with methanol competing for channel sites while lattice –OH is unchanged. Under methanol, the C–H (2950–2850 cm^{-1}) envelope and the ~1470 cm^{-1} band both attenuate after 24 h and remain low at 72 h, consistent with partial removal/oxidation of native organic impurities residues rather than buildup of methanol-derived layers. In water-only reference, both the C–H region and ~1470 cm^{-1} grow, indicating UV-driven redistribution and possible partial cross-linking of aliphatic fragments at the outer surface (with possible CO_3/CH overlap near ~1384 cm^{-1}) [8]. The H–O–H bend (~1660, 1630 cm^{-1}) intensity declines when reaction was performed in aqueous methanol but intensifies in sample exposed to water [2,5,8]; δCO_3 near ~880 cm^{-1} is absent [9]. The framework is unchanged: ν_{as}(Si–O–Si) (~1250–1190 cm^{-1}), ν(Si–O) (~1080; ~1020, 980 cm^{-1}) and lattice modes (~780, 690–650, 540 cm^{-1}) retain positions and overall profiles corroborating T–O–T ribbon invariance [2–5,12]. Quantitatively, the integrated O–H area rises from 158.7 (native) to 180.9 (24 h) and 199.0 (72 h); the water-only reference reaches 244.0. The O–H FWHM (full width at half minimum) broadens from 359.4 cm^{-1} (native) to 382.9 cm^{-1} (24 h) and 375.3 cm^{-1} (72 h); the blank is 355.6 cm^{-1}. Thus, PLG shows progressive channel/edge hydration together with removal of native organics, yielding a more accessible yet structurally undisturbed surface. Integrated O–H area increases continuously from native to 72 h and is maximal in the water-only reference, showing progressive surface cleaning and hydration; methanol competes with water, so total O–H loading is lower than in pure water. In aqueous methanol, the O–H peak gets wider (larger FWHM), which means the surface has a more heterogeneous set of H-bonds from co-adsorbed water/methanol and possibly UV-formed species. By contrast, the water blank shows a narrower band, consistent with a more uniform water H-bond network. XRD peak invariance rules out lattice change—these are surface-chemical effects.

UV-C pretreatment can raise the number/accessibility of surface –OH groups on inorganic surfaces; such hydroxylated interfaces are known to shuttle protons rapidly to nearby molecules. Together, this makes faster proton transfer—and thus easier alcohol activation—plausible for PLG post UV-C pretreatment [18–20].

2.3. UV-Vis Diffuse Reflectance

The UV–Vis diffuse reflectance spectra of sepiolite (SEP) and palygorskite (PLG) were analyzed to evaluate their optical response and to estimate the apparent optical gap of the studied materials. For this purpose, the reflectance data were converted using the Kubelka–Munk formalism and interpreted using Tauc plots. The corresponding results are presented in Figure S4

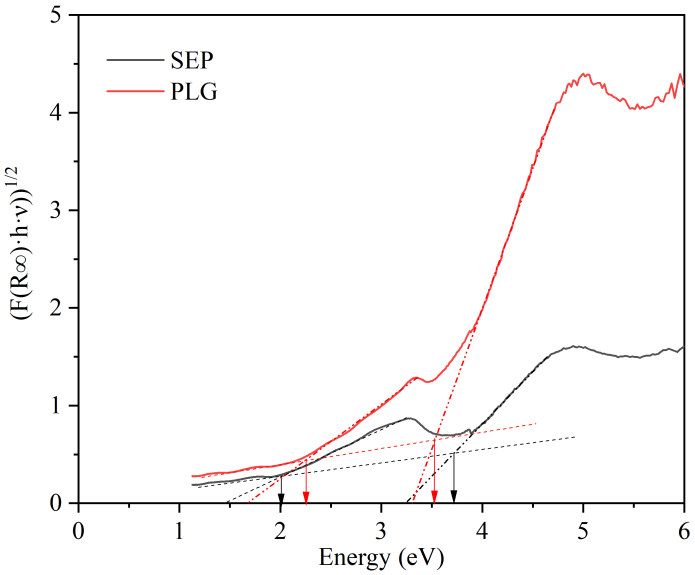

Figure S4. Tauc plots for sepiolite (SEP, black) and palygorskite (PLG, red) derived from UV-Vis DRS illustrating the evaluation of apparent (model-dependent) optical gap parameters.

2.4. Photocatalytic Methanol Reforming

The photocatalytic performance of the studied materials in methanol reforming was assessed by measuring hydrogen evolution as a function of irradiation time. Native sepiolite (SEP), palygorskite (PLG), and TiO_2 (P25) were compared with the corresponding samples subjected to 24 h of UVC pretreatment in order to evaluate the effect of irradiation-induced changes on photocatalytic activity. The time-dependent hydrogen yields are presented in Figure S5.

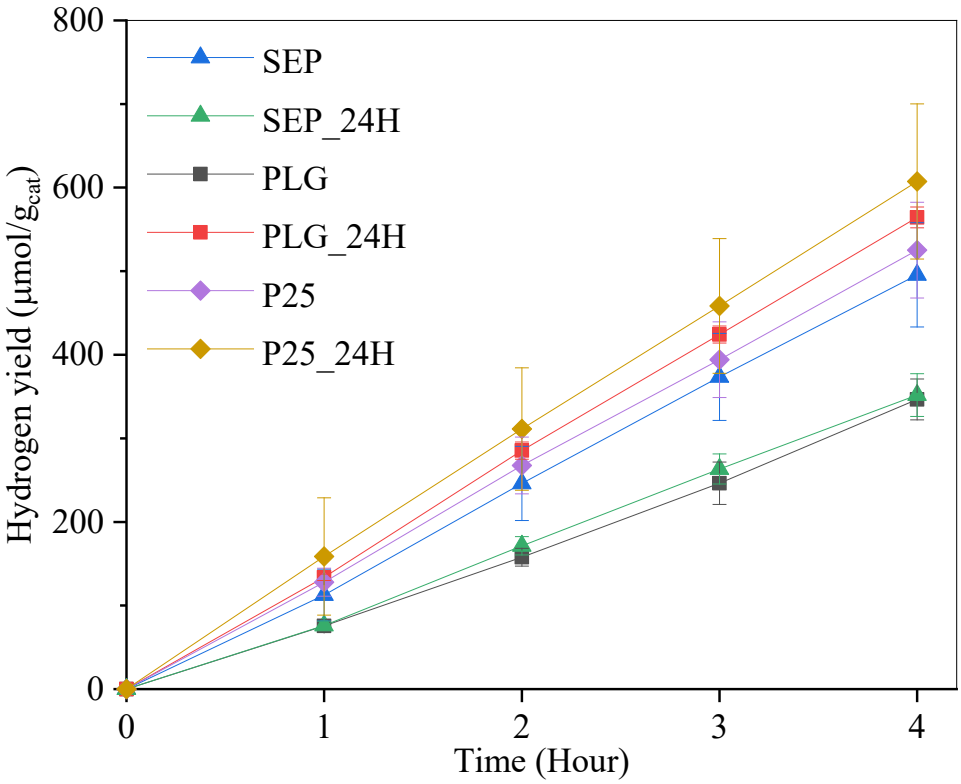

Figure S5. Time-dependent hydrogen evolution of sepiolite (SEP), palygorskite (PLG), and TiO_2 (P25) photocatalysts before and after 24 h of UV-C pretreatment (24 h) in aqueous methanol under continuous irradiation.

References

1. Serna, C.; Ahlrichs, J.L.; Serratosa, J.M. Folding in Sepiolite Crystals. *Clays Clay Miner.* **1975**, *23*, 452–457. https://doi.org/10.1346/CCMN.1975.0230607.
2. Madejová, J.; Gates, W.P.; Petit, S. IR Spectra of Clay Minerals. In *Developments in Clay Science*; Elsevier: Amsterdam, The Netherlands, 2017; Volume 8, pp 107–149. https://doi.org/10.1016/B978-0-08-100355-8.00005-9.
3. Lescano, L.; Castillo, L.; Marfil, S.; et al. Alternative Methodologies for Sepiolite Defibering. *Appl. Clay Sci.* **2014**, *95*, 378–382. https://doi.org/10.1016/j.clay.2014.05.001.
4. Bukas, V.J.; Tsampodimou, M.; Gionis, V.; et al. Synchronous ATR Infrared and NIR-Spectroscopy Investigation of Sepiolite upon Drying. *Vib. Spectrosc.* **2013**, *68*, 51–60. https://doi.org/10.1016/j.vibspec.2013.05.009.
5. Frost, R.L.; Locos, O.B.; Ruan, H.; et al. Near-Infrared and Mid-Infrared Spectroscopic Study of Sepiolites and Palygorskites. *Vib. Spectrosc.* **2001**, *27*, 1–13. https://doi.org/10.1016/S0924-2031(01)00110-2.
6. Walczyk, A.; Karcz, R.; Kryściak-Czerwenka, J.; et al. Influence of Dry Milling on Phase Transformation of Sepiolite upon Alkali Activation: Implications for Textural, Catalytic and Sorptive Properties. *Materials* **2020**, *13*, 3936. https://doi.org/10.3390/ma13183936.
7. Prost, R. Infrared Study of the Interactions between the Different Kinds of Water Molecules Present in Sepiolite. *Spectrochim. Acta, Part A* **1975**, *31*, 1497–1499. https://doi.org/10.1016/0584-8539(75)80206-6.
8. Margenot, A.J.; Parikh, S.J.; Calderón, F.J. Fourier-Transform Infrared Spectroscopy for Soil Organic Matter Analysis. *Soil Sci. Soc. Am. J.* **2023**, *87*, 1503–1528. https://doi.org/10.1002/saj2.20583.
9. Gunasekaran, S.; Anbalagan, G.; Pandi, S. Raman and Infrared Spectra of Carbonates of Calcite Structure. *J. Raman Spectrosc.* **2006**, *37*, 892–899. https://doi.org/10.1002/jrs.1518.
10. Veerasingam, S.; Venkatachalapathy, R. Estimation of Carbonate Concentration and Characterization of Marine Sediments by Fourier Transform Infrared Spectroscopy. *Infrared Phys. Technol.* **2014**, *66*, 136–140. https://doi.org/10.1016/j.infrared.2014.06.005.
11. Gionis, V. On the Structure of Palygorskite by Mid- and Near-Infrared Spectroscopy. *Am. Mineral.* **2006**, *91*, 1125–1133. https://doi.org/10.2138/am.2006.2023.
12. McKeown, D.A.; Post, J.E.; Etz, E.S. Vibrational Analysis of Palygorskite and Sepiolite. *Clays Clay Miner.* **2002**, *50*, 667–680. https://doi.org/10.1346/000986002320679549.
13. Yan, W.; Liu, D.; Tan, D.; et al. FTIR Spectroscopy Study of the Structure Changes of Palygorskite under Heating. *Spectrochim. Acta Part A* **2012**, *97*, 1052–1057. https://doi.org/10.1016/j.saa.2012.07.085.
14. Bourliva, A.; Sikalidis, A.K.; Papadopoulou, L.; et al. Removal of Cu^{2+} and Ni^{2+} Ions from Aqueous Solutions by Adsorption onto Natural Palygorskite and Vermiculite. *Clay Miner.* **2018**, *53*, 1–15. https://doi.org/10.1180/clm.2017.1.
15. Liu, Q.; Yao, X.; Cheng, H.; et al. An Infrared Spectroscopic Comparison of Four Chinese Palygorskites. *Spectrochim. Acta Part A* **2012**, *96*, 784–789. https://doi.org/10.1016/j.saa.2012.07.025.
16. Suárez, M.; García-Romero, E. FTIR Spectroscopic Study of Palygorskite: Influence of the Composition of the Octahedral Sheet. *Appl. Clay Sci.* **2006**, *31*, 154–163. https://doi.org/10.1016/j.clay.2005.10.005.
17. Frost, R.L.; Cash, G.A.; Kloprogge, J.T. 'Rocky Mountain Leather', Sepiolite and Attapulgite—An Infrared Emission Spectroscopic Study. *Vib. Spectrosc.* **1998**, *16*, 173–184. https://doi.org/10.1016/S0924-2031(98)00014-9.
18. Pavan, C.; Santalucia, R.; Escolano-Casado, G.; et al. Physico-Chemical Approaches to Investigate Surface Hydroxyls as Determinants of Molecular Initiating Events in Oxide Particle Toxicity. *Int. J. Mol. Sci.* **2023**, *24*, 11482. https://doi.org/10.3390/ijms241411482.
19. Kobayashi, T.; Ikeda, T.; Nakayama, A. Long-Range Proton and Hydroxide Ion Transfer Dynamics at the Water/CeO_2 Interface in the Nanosecond Regime: Reactive Molecular Dynamics Simulations and Kinetic Analysis. *Chem. Sci.* **2024**, *15*, 6816–6832. https://doi.org/10.1039/D4SC01422G.
20. Ichikawa, T.; Yamada, T.; Aoki, N.; et al. Surface Proton Hopping Conduction Mechanism Dominant Polymer Electrolytes Created by Self-Assembly of Bicontinuous Cubic Liquid Crystals. *Chem. Sci.* **2024**, *15*, 7034–7040. https://doi.org/10.1039/D4SC01211A.